INTERNATIONAL JOURNAL FOR NUMERICAL METHODS IN FLUIDS
*Int. J. Numer. Meth. Fluids* 2003; **42**:885–908 (DOI: 10.1002/fld.556)

# Adaptive strategy of transonic flows over vibrating blades with interblade phase angles

S. Y. Yang*,†

*Department of Aeronautical Engineering, National Huwei Institute of Technology, Huwei, Yunlin 632, Taiwan, R.O.C.*

## SUMMARY

An error indicator and a locally implicit scheme with anisotropic dissipation model on dynamic quadrilateral–triangular mesh are developed to study transonic flows over vibrating blades with interblade phase angles. In the Cartesian co-ordinate system, the unsteady Euler equations with moving domain effects are solved. The error indicator, in which unified magnitudes of dynamic grid speed, substantial derivative of pressure, and substantial derivative of vorticity magnitude are incorporated to capture the unsteady wave behaviours and vortex-shedding phenomena due to unsteadiness. To assess the accuracy of the locally implicit scheme with anisotropic dissipation model on quadrilateral–triangular mesh, two flow calculations are performed. Based on the comparison with the related numerical and experimental data, the accuracy of the present approach is confirmed. According to the high-resolutional result on the adaptive mesh, the unsteady pressure wave, shock and vortex-shedding behaviours are clearly demonstrated. Copyright © 2003 John Wiley & Sons, Ltd.

KEY WORDS: error indicator; vibrating blades; interblade phase angles

## 1. INTRODUCTION

Unsteady aerodynamic behaviour has attracted increasing interest in the development of new turbomachinery. For solving oscillating cascade flows, the linearized models, such as the linearized potential [1] and Euler [2] solvers have been used. Although linearized methods meet the need for efficient unsteady aerodynamic response predictions, their validity is limited by the linear assumption. As mentioned by Wolff and Fleeter [3], non-linear effects were quite likely to be associated with larger amplitudes of blade oscillation as well as unsteady transonic flows with shock motion induced by oscillating blades at small amplitudes. In recent years, a number of Euler [3–9] and Navier–Stokes [8–12] solvers have been presented to simulate the blade vibration problems. To save computing effort, He [4] developed a zonal moving grid technique in which only subregions near oscillating blades were moved. Huff [5] proposed

---

*Correspondence to: S. Y. Yang, Department of Aeronautical Engineering, National Huwei Institute of Technology, Huwei, Yunlin 632, Taiwan, R.O.C.
†E-mail: anneyang@sunws.nhit.edu.tw

*Received 22 May 2002*
*Revised 11 March 2003*

a deforming grid treatment to create C-grids, where the multiple blade computational mesh was accomplished by stacking C-grids for each blade. To confine the computational domain within single-blade passage for arbitrary interblade phase angle values, Wolff and Fleeter [3] applied the Fourier series lagged boundary condition treatment on an expanded grid along the periodic boundary. Actually, the periodic boundary became part of the interior solution. On a quadrilateral–triangular mesh, Hwang and Yang [6] presented a rigid-deformable dynamic mesh algorithm to investigate transonic flows around an oscillating cascade of four blades. A three-dimensional Euler Solver [7] for vibrating cascade aerodynamics, in which a space-centred finite volume scheme and a five-stage Runga–Kutta integration procedure were used, had been validated by comparison with available theoretical and semi-analytical results. The time-accurate Euler/Navier–Stokes analysis [8] using NPHASE code [9] was applied, and computed results were compared with those based on linearized LINFLO code [13]. To solve the three-dimensional thin-layer Navier–Stokes equations in a simplified form, a time-consistent two-grid time marching technique [10] is adopted to relax the time-step limitation of explicit Runge–Kutta scheme. On a multi-passage computational mesh [11], the explicit four-stage Runge–Kutta scheme and the Baldwin–Lomax mixing length turbulence model were adopted. The calculation showed that there was a more apparent mesh dependence of the results in the regions of flow separation. A coupled viscous/inviscid code [12] in which the thin-layer Navier–Stokes equations were solved on an inner O-grid around each blade, while the Euler equations were solved on the outer unstructured mesh. Before the beginning of unsteady calculation, the outer triangular mesh was adapted according to the steady-state solution. This steady adapted mesh was used throughout the entire unsteady calculation. On a composite grid where a deforming C-grid was embedded in an H-grid, a coupled inviscid/viscous model [14] was implemented to incorporate the inverse integral boundary layer solution and the time-marching NPHASE analysis. It was indicated [15] that oscillating magnitude and steady loading had a significant effect on both the influence coefficient data and the equivalent all-airfoils-oscillating data.

As mentioned by Sheng *et al.* [16] the biggest advantage of the unstructured grid approach over the structured grid approach was that the process of grid generation for complex geometries was greatly simplified. Also mentioned by Mavriplis [17], unstructured grid techniques offered the potential for greatly reducing the grid generation time associated with complex geometries. Furthermore, unstructured mesh approaches enabled the use of adaptive meshing techniques, which held great promise for increasing solution accuracy at minimal additional computational cost. Recently, considerable effort has been made to develop solution-adaptive techniques [18–25] for solving the Euler/Navier–Stokes equations on unstructured meshes. The mesh-enrichment and mesh-coarsening procedures [18] were implemented within an unstructured grid upwind-type Euler code, and the absolute value of the substantial derivative of density was used as an enrichment indicator. By using the two-step Runge–Kutta Galerkin finite-element method and a local remeshing technique [19], a shock propagation within a channel was investigated. From the time-varying meshes, directionally stretched elements were demonstrated. Webster *et al.* [20] developed an adaptive finite-element methodology, in which the finite quadtree mesh generator, interpolation-based error indicator and edge-based mesh enrichment procedure were employed. On a fully unstructured mesh of tetrahedral elements, a solution adaptive multigrid scheme [21] was developed to study the transonic flows about an aircraft engine nacelle. A general adaptation procedure [22] based on h-refinement and coarsening was developed to improve the resolution of complex flow features. By discretizing the flow domain with both prismatic and tetrahedral elements, a hybrid grid adaptive algorithm [23] that combined grid refinement and redistribution was presented. A grid refinement technique [24], which was based on a combination of surface mesh subdivision and local remeshing of the volume grid, was developed and successfully applied to several three-dimensional flow test cases. Walsh and Zingg [25] presented a solution-dependent retriangulation algorithm which locally restructured the grid to recover an anisotropic grid following adaptation. An adaptive refinement strategy [26] based on hierarchical subdivision was formulated and implemented for meshes containing arbitrary mixtures of tetrahedral, hexahedra, prisms, and pyramids. Yang [27] presented an error indicator in which the unified magnitude of pressure gradient and unified magnitude of gradient of vorticity magnitude were incorporated to study the supersonic flow over a backward-facing step.

There are three objectives in the present study: (1) To develop an error indicator for dynamic flows dominated by unsteady pressure wave, shock and vortex; (2) To develop the locally implicit scheme with anisotropic dissipation model on dynamic quadrilateral–triangular mesh; and (3) To investigate transonic flows over vibrating blades with interblade phase angles.

## 2. GOVERNING EQUATIONS

The two-dimensional Euler equations with moving domain effects in the Cartesian co-ordinate system can be written as

$$\frac{\partial U}{\partial t} + \nabla \cdot \mathbf{F} = 0 \tag{1}$$

where $\mathbf{F} = E\mathbf{i} + G\mathbf{j}$

$$U = \begin{bmatrix} \rho \\ \rho u \\ \rho v \\ e \end{bmatrix}, \quad E = \begin{bmatrix} \rho(u - x_t) \\ \rho u(u - x_t) + p \\ \rho(u - x_t)v \\ e(u - x_t) + pu \end{bmatrix}, \quad G = \begin{bmatrix} \rho(v - y_t) \\ \rho u(v - y_t) \\ \rho v(v - y_t) + p \\ e(v - y_t) + pv \end{bmatrix}$$

Variables $\rho$, $u$, $v$ and $e$ represent the gas density, velocity component in $x$, $y$ directions and total energy per unit volume, respectively. $x_t$ and $y_t$ are the grid speeds in the $x$ and $y$ directions, respectively. Pressure $P$ is given by the equation of state, and $\gamma$ is the ratio of specific heat.

$$P = (\gamma - 1)\left[e - \frac{\rho}{2}(u^2 + v^2)\right] \tag{2}$$

By integrating Equation (1) over space and using Gauss's theorem, the following expression is obtained:

$$\frac{\partial}{\partial t}\iint_{\Omega} U \, \mathrm{d}A + \int_{\partial\Omega} \mathbf{F} \cdot \mathrm{d}\mathbf{l} = 0 \tag{3}$$

where $\mathrm{d}\mathbf{l} = \mathbf{n}\,\mathrm{d}\ell$, and $\mathbf{n}$ is the unit normal vector in the outward direction. $\Omega$ is the moving domain of interest and $\partial\Omega$ is the boundary of domain. A fully implicit finite-volume discretization scheme is applied to Equation (3) over the entire flowfield. Flow variables at cell faces are obtained from the averages of flow variables at the cell centres. Those values and artificial dissipation terms are introduced for line integral and numerical stability. By implementing a two-parameter family $(\theta, \beta)$ on the dynamic quadrilateral–triangular mesh, Equation (3) can be written as

$$\begin{aligned}
&\left(\frac{A^{n+1}\Delta U^n}{\Delta t}\right)_i + \frac{\theta}{1+\beta} Q_i(U^{n+1}) - \frac{\theta}{1+\beta} D_i(U^{n+1}) \\
&\quad = -\frac{1-\theta}{1+\beta} Q_i(U^n) + \frac{1-\theta}{1+\beta} D_i(U^n) + \frac{\beta}{1+\beta}\left(\frac{A^n \Delta U^{n-1}}{\Delta t}\right)_i \\
&\qquad - \left(\frac{U^n \Delta A^n}{\Delta t}\right)_i + \frac{\beta}{1+\beta}\left(\frac{U^{n-1}\Delta A^{n-1}}{\Delta t}\right)_i
\end{aligned} \tag{4}$$

where

$$\begin{aligned}
\Delta U^n &= U^{n+1} - U^n \\
\Delta A^n &= A^{n+1} - A^n \\
Q_i(U) &= \sum_{k=1}^{N_i} (\mathbf{F} \cdot \mathbf{dl})_{ik} \\
N_i &= \begin{cases} 3 & \text{for triangular cell } i \\ 4 & \text{for quadrilateral cell } i \end{cases}
\end{aligned}$$

$A_i$, $n$, and $D_i$ represent the cell area, marching time step and artificial dissipation operator, respectively. In this paper, $\theta = 1$ and $\beta = 0$ are selected for steady flow calculations and the scheme becomes first-order accurate in time, whereas $\theta = 1$ and $\beta = \frac{1}{2}$ are adopted for unsteady flow calculations and the scheme becomes second-order accurate in time. The fourth and fifth terms on the right-hand side of Equation (4) account for the effects of area variation when meshes deform during time evolution. Under rigid-body motions or mesh-fixed situations, these two terms will vanish.

On the structured grid system, Jameson *et al.* [28] developed an effective form for $D_i$. The isotropic value for scaling the dissipation has been extended to unstructured triangular meshes by Mavriplis [29]. On the static triangular mesh, Hwang and Liu [30] developed the anisotropic dissipation model. In this article, the anisotropic dissipation model will be extended to the dynamic quadrilateral–triangular mesh. The mathematical form is described as follows:

$$D_i(U) = \sum_{k=1}^{N_i} d_{ik} \tag{5}$$

where

$$\begin{aligned}
d_{ik} &= \varepsilon_{ik}^{(2)}(U_k - U_i) - \varepsilon_{ik}^{(4)}(\nabla^2 U_k - \nabla^2 U_i) \\
\varepsilon_{ik}^{(2)} &= k^{(2)} \psi_{ik} \bar{v}_{ik}
\end{aligned}$$

$$
\begin{aligned}
\varepsilon_{ik}^{(4)} &= k^{(4)}\psi_{ik}\max[0,(1-32\bar{v}_{ik})]\\
\psi_{ik} &= (|(\mathbf{V}-\mathbf{V}_{\mathrm{g}})\cdot\mathrm{d}\mathbf{l}| + a|\mathrm{d}\mathbf{l}|)_{ik}\\
v_{ik} &= \frac{|\nabla^2 p_i|}{\sum_{k=1}^{N_i}(p_i+p_k)}\\
\bar{v}_{ik} &= \begin{cases}\max(v_i, v_k, v_{k_1}, v_{k_2}, v_{k_3}), & N_k = 3\\ \max(v_i, v_k, v_{k_1}, v_{k_2}, v_{k_3}, v_{k_4}), & N_k = 4\end{cases}\\
\nabla^2 U_i &= \sum_{k=1}^{N_i} U_k - N_i U_i\\
\mathbf{V} &= u\mathrm{i} + v\mathrm{j}\\
\mathbf{V}_{\mathrm{g}} &= x_t\mathbf{i} + y_t\mathbf{j}
\end{aligned}
$$

Subscripts $k_1$, $k_2$ and $k_3$ represent the indices of three adjacent cells which surround the triangular cell $k$, whereas subscripts $k_1$, $k_2$, $k_3$ and $k_4$ represent the indices of four adjacent cells which surround the quadrilateral cell $k$. $\nabla^2 U_i$ is expressed as undivided Laplacian operator. $\psi_{ik}$ is the spectral radius of Jacobian matrix $(\partial\mathbf{F}/\partial U\cdot\mathrm{d}\mathbf{l})$ on the interface between cell $i$ and cell $k$. Two constants $k^{(2)}$ and $k^{(4)}$ are taken as $\frac{1}{4}$ and $\frac{1}{64}$, respectively.

By using a Taylor series expansion for temporal differences, Equation (4) is linearized and can be constructed in the delta form as follows:

$$
\begin{aligned}
L_i(\Delta U^n) = Res_i^n = &-\frac{1}{1+\beta}Q_i(U^n) + \frac{1}{1+\beta}D_i(U^n) + \frac{\beta}{1+\beta}\left(\frac{A^n\Delta U^{n-1}}{\Delta t}\right)_i\\
&-\left(\frac{U^n\Delta A^n}{\Delta t}\right)_i + \frac{\beta}{1+\beta}\left(\frac{U^{n-1}\Delta A^{n-1}}{\Delta t}\right)_i\\
&-\frac{\theta}{2(1+\beta)}\sum_{k=1}^{N_i}[(\mathbf{F}_i+\mathbf{F}_k)^n\cdot(\mathrm{d}\mathbf{l}^{n+1}-\mathrm{d}\mathbf{l}^n)]
\end{aligned}
\tag{6}
$$

where

$$
\begin{aligned}
L_i(\Delta U^n) &= CI\,\Delta U_i^n + \sum_{L=1}^{N_i} CK_L\,\Delta U_L^n + \frac{\theta}{1+\beta}\sum_{k=1}^{N_i}\varepsilon_{ik}^{(4)}\sum_{j=1}^{N_i}\Delta U_j^n\\
CI &= \frac{\theta}{2(1+\beta)}\left(\sum_{k=1}^{N_i}M_{ik}\right) + \frac{\theta}{1+\beta}\left(\sum_{k=1}^{N_i}\varepsilon_{ik}^{(2)} + N_i\sum_{k=1}^{N_i}\varepsilon_{ik}^{(4)}\right)I + \left(\frac{A^{n+1}}{\Delta t}\right)_i I\\
CK_L &= \frac{\theta}{2(1+\beta)}M_{iL} - \frac{\theta}{1+\beta}\left(\varepsilon_{iL}^{(2)} + N_L\varepsilon_{iL}^{(4)} + \sum_{k=1}^{N_i}\varepsilon_{ik}^{(4)}\right)I\\
I &= \mathrm{Diag}[1,1,1,1]\\
M_{ik} &= \left(\frac{\partial\mathbf{F}^n}{\partial U}\cdot\mathrm{d}\mathbf{l}^{n+1}\right)_{ik}
\end{aligned}
$$

The last term on the right-hand side of Equation (6) arises from the dynamic mesh effects during linearization. To solve Equation (6), a locally implicit scheme [31, 32] is implemented. This scheme is locally implicit, but globally explicit and is unconditionally stable under local linearized analysis [32]. It does not require the assembly of any global matrices and does not need any matrix system solvers. The locally implicit scheme is originally developed by Reddy and Jacock [31] on structured quadrilaterals. Hwang and Liu [30] developed the locally implicit scheme and anisotropic dissipation model on the static triangular mesh. In this paper, the locally implicit scheme and anisotropic dissipation model is extended to the dynamic quadrilateral–triangular mesh.

For each cell $i$, the equation for iterative corrections is written as

$$C dU_i = Re\, s_i^n - L_i(\Delta U) \tag{7}$$

$$\Delta U_i^{(m+1)} = \Delta U_i^{(m)} + W_{\text{in}}\, \mathrm{d}U_i, \quad m = 1, 2 \tag{8}$$

where $C$ is a diagonal matrix defined as a modification to the coefficient $CI$

$$C = \left(\frac{A^{n+1}}{\Delta t}\right)_i \left[1.0 + \frac{\theta}{2(1+\beta)} CFL\right] I + \left[\frac{\theta}{1+\beta}\left(\sum_{k=1}^{N_i} \varepsilon_{ik}^{(2)} + N_i \sum_{k=1}^{N_i} \varepsilon_{ik}^{(4)}\right)\right] I \tag{9}$$

where $CFL$ is the Courant–Friedrichs–Lewy number. $\Delta U$ shown on the right-hand side of Equation (7) takes the latest available values from Equation (8). The inner iteration for $\Delta U^{(m+1)}$ can be computed rapidly since the $\mathrm{d}U$ corrections are explicit scalar equations. One symmetric cycle of inner iterations is employed in each time step for steady flow calculations, whereas several cycles are performed until a convergence state of $\Delta U_i^{(m+1)}$ is reached for unsteady flow calculations. At the end of a time step, the outer relaxation is introduced.

$$U_i^{n+1} = U_i^n + W_{\text{out}} \Delta U_i \tag{10}$$

The coefficients $W_{\text{in}}$ and $W_{\text{out}}$ in Equations (8) and (10) are inner and outer relaxation parameters, respectively, of order 1.2 for steady flow calculations, whereas $W_{\text{out}}$ is set to be 1.0 for unsteady flow calculations.

## 3. ADAPTIVE-MESH ALGORITHM

The present adaptive algorithm includes the error indicator and two-level refinement technique. As for the selection of error indicator, Rausch *et al.* [18] adopted the absolute value of substantial derivative of density $|\mathrm{D}\rho/\mathrm{D}t|$ as the error indicator to simulate unsteady inviscid flow problems. In the author's previous study [27], an error indicator, which incorporated the unified magnitude of pressure gradient ($|\nabla p|$) and unified magnitude of gradient of vorticity magnitude ($|\nabla\omega|$, vorticity magnitude $\omega = |\nabla \times \mathbf{V}|$), was proposed and formulated as

$$\mathrm{EI} = \frac{|\nabla P|}{|\nabla P|_{\max}} + \beta \frac{|\nabla \omega|}{|\nabla \omega|_{\max}} \tag{11}$$

Based on the comparison of the adaptive meshes [27] obtained using Equation (11) and the other three different error indicators which were absolute values of density gradient $|\nabla\rho|$, Mach number gradient $|\nabla M|$ and gradient of vorticity magnitude $|\nabla \omega|$, the error indicator in Equation (11) could incorporate the advantages and avoid the disadvantages of the other three error indicators for flows dominated by pressure wave and vortex.

In the present study, the error indicator in Equation (11) is further improved to account for the unsteadiness and dynamic grid effect. The present error indicator is formulated as

$$\mathrm{EI} = \frac{|\mathrm{D}P/\mathrm{D}t|}{|\mathrm{D}p/\mathrm{D}t|_{\max}} + \beta_1 \frac{|\mathrm{D}\omega/\mathrm{D}t|}{|\mathrm{D}\omega/\mathrm{D}t|_{\max}} + \beta_2 \frac{|\mathbf{V}_{\mathrm{g}}|}{|\mathbf{V}_{\mathrm{g}}|_{\max}} \tag{12}$$

where $|\mathrm{D}p/\mathrm{D}t|$, $|\mathrm{D}\omega/\mathrm{D}t|$ and $|\mathbf{V}_{\mathrm{g}}|$ are the absolute values of the substantial derivative of pressure, substantial derivative of vorticity magnitude, and velocity vector of dynamic grid, respectively. $|\mathrm{D}p/\mathrm{D}t|_{\max}$, $|\mathrm{D}\omega/\mathrm{D}t|_{\max}$ and $|\mathbf{V}_{\mathrm{g}}|_{\max}$ are the maximum values of $|\mathrm{D}p/\mathrm{D}t|$, $|\mathrm{D}\omega/\mathrm{D}t|$ and $|\mathbf{V}_{\mathrm{g}}|$ among all the computational cells, respectively. Since the order of magnitude of $|\mathrm{D}\omega/\mathrm{D}t|$ outnumbers those of $|\mathrm{D}p/\mathrm{D}t|$ and $|\mathbf{V}_{\mathrm{g}}|$, it is essential to adjust all at the same order. Hence, $|\mathrm{D}p/\mathrm{D}t|$, $|\mathrm{D}\omega/\mathrm{D}t|$ and $|\mathbf{V}_{\mathrm{g}}|$ are divided by $|\mathrm{D}p/\mathrm{D}t|_{\max}$, $|\mathrm{D}\omega/\mathrm{D}t|_{\max}$ and $|\mathbf{V}_{\mathrm{g}}|_{\max}$, respectively. $\beta_1$ and $\beta_2$ represents the weighted coefficients. For the calculations of transonic flows over vibrating blades, $\beta_1$ and $\beta_2$ and are set to be 2.0 and 1.0, respectively.

As for the two-level refinement technique, the mesh enrichment is operated on the background grid (initial grid) instead of the last adapted mesh. Therefore, the number of cells will not increase unlimitedly during adaptations. At first, the value of EI of each unrefined cell is firstly calculated. The product of a specified constant $C_1$ and the average value of EI over the initial grid is selected as the first threshold value. If the value of EI of each unrefined cell is larger than the first threshold value $C_1 * \mathrm{EIave}$, the new node will be placed at the mid-point of each edge of quadrilateral/triangular cell or the centre of quadrilateral cell [33]. After finishing the first-level refinement, the properties at all added new cells are interpolated from those at the initial grid. Continuing the second-level mesh refinement, the value of EI for each cell on the intermediate mesh and the corresponding second threshold value $C_2 * \mathrm{EIave}$ are computed. It is not necessary to perform any Euler iteration between level 1 and level 2 refinements. Normally, the value of constant $C_2$ is about three times bigger than that of constant $C_1$, and the value of constant $C_1$ is ranged from 0.4 to 0.8. In the present calculation, $C_1$ and $C_2$ are chosen as 0.6 and 1.8, respectively. Then the intermediate mesh is refined by reprocessing the first-level refinement technique. Since Webster *et al.* [20] mentioned that the mesh coarsening accounted for the majority of CPU cost during adaptation, the mesh coarsening procedure is not processed in this article.

## 4. BOUNDARY CONDITIONS

For the steady flow calculations, no-penetration and adiabatic wall conditions are imposed at the body or wall surface. Pressure is obtained by the following condition:

$$\rho(y_\eta u - x_\eta v)(y_\xi u_\xi - x_\xi v_\xi) = (x_\xi^2 + y_\xi^2)P_\eta - (x_\xi x_\eta + y_\xi y_\eta)P_\xi \tag{13}$$

where $\eta$ and $\xi$ represent the body-fitted co-ordinate lines. Density is obtained from the equation of state. As for the far field of transonic flow around an NACA 0012 airfoil, one-dimensional characteristic analysis based on Riemann invariants is used to determine the values of flow variables on the outer boundary of the computational domain.

For the unsteady calculations of transonic flows over vibrating blades with interblade phase angles, no penetration condition with respect to the moving blade is imposed on the vibrating blade surfaces. Pressure, density and velocity components parallel to the moving surface are obtained by extrapolation from the values at interior cells. On the upper and lower periodic boundaries, the same number of cells and nodes are generated during adaptation. The nodes on both of the upper and lower boundaries are located at the same position along the $X$-axis, but with a fixed distance in the $Y$-axis, which is equal to the height of computational domain. Therefore, both the corresponding cells at upper and lower periodical boundaries are assigned to the neighbours of each other, and they are treated as interior cells. The dynamic mesh algorithm [34] is applied in this paper. Based on the Gauss–Seidel method, the displacement of each interior node is obtained by solving the static equilibrium equations. At the inlet and outlet boundaries, two-dimensional unsteady non-reflecting boundary condition, which was developed by Giles [35], is utilized.

In addition to the mass, momentum and energy conservation laws that govern the physics of the flow, the geometric conservation [36, 37] is stated as follows:

$$\frac{\partial}{\partial t}\iint_{\Omega} \mathrm{d}A = \int_{\partial\Omega} \mathbf{V}_{\mathrm{g}} \cdot \mathrm{d}\mathbf{l} \tag{14}$$

after discretization, Equation (14) can be written as

$$\frac{\delta A_j}{\Delta t} = (\mathbf{V}_{\mathrm{g}} \cdot \mathrm{d}\mathbf{l})_j \tag{15}$$

and

$$A_i^{n+1} - A_i^n = \sum_{j=1}^{N_i} \delta A_j \tag{16}$$

where $A_i^{n+1}$ and $A_i^n$ denote the cell areas at new and old time levels, respectively. $\delta A_j$ represents the area change due to the movement of the $j$th cell edge during time interval $\Delta t$, and $N_i$ is set to be 3 or 4 for triangular or quadrilateral cell $i$, respectively. In the present dynamic solver, the new mesh positions are obtained from the dynamic mesh algorithm [34], and the area $\delta A_j$ is determined from new and old mesh positions. The flux due to grid speed across $j$th cell boundary $(\mathbf{V}_{\mathrm{g}} \cdot \mathrm{d}\mathbf{l})_j$, which has appeared in Equation (3), is determined from Equation (15). It is noted that $(\mathbf{V}_{\mathrm{g}} \cdot \mathrm{d}\mathbf{l})_j$ has been averaged with respect to time and $(\mathbf{V}_{\mathrm{g}})_j$ is not necessary to be calculated.

## 5. RESULTS AND DISCUSSION

On quadrilateral–triangular meshes, the capability of the locally implicit scheme with anisotropic dissipation model developed in this paper is evaluated by performing two steady flow calculations, which include the oblique shock reflection at a wall and transonic flow around an NACA 0012 airfoil. To further demonstrate the versatility of the present error indicator, the transonic flows over vibrating blades with interblade phase angles are investigated.

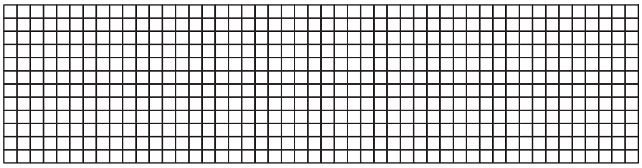

Figure 1. Initial mesh of oblique shock reflection at a wall (576 cells).

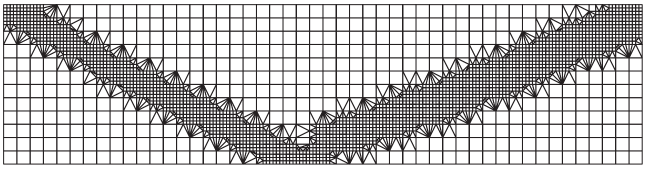

Figure 2. Adaptive mesh of oblique shock reflection at a wall (3016 cells).

### *5.1. Oblique shock reflection at a wall*

In this flow problem, the freestream Mach number and incident shock angle are equal to 2.9 and 29°, respectively. The initial mesh shown in Figure 1 is the structured quadrilateral grid, which is treated in an unstructured manner. After obtaining the steady-state solution on the initial mesh, the adaptive quadrilateral–triangular mesh shown in Figure 2 is achieved according to the steady solution, where both $\beta_1$ and $\beta_2$ in Equation (12) are set to be 0.0. On the adaptive quadrilateral–triangular mesh, the incident and reflective shocks are clearly resolved. Pressure distributions on the wall including the exact solution, steady solutions on both initial and adaptive meshes are plotted in Figure 3. From Figure 3, the high-resolutional result that is obtained on the adaptive mesh compares well with the exact solution. In this article, steady-state solutions are assumed to be achieved when the $L_2$-norm of density is less than or equal to $10^{-6}$.

### *5.2. Transonic flow around an NACA 0012 airfoil*

To further evaluate the locally implicit scheme with anisotropic dissipation model on mixed mesh, transonic flow ($M_\infty = 0.8$) around an NACA 0012 airfoil with angle of attack ($\alpha = 1.25°$) is investigated. The computational domain is taken to be $21C \times 20C$, where $C$ is the chord length. The initial quadrilateral–triangular mesh system (see Figure 4) contains 4688 cells and 3285 nodes, and there are 110 points that lie on the airfoil surface. Again, the adaptive mesh shown in Figure 5 is achieved according to the steady solution on initial mesh, where both $\beta_1$ and $\beta_2$ in Equation (12) are set to be 0.0. Pressure coefficient distributions on the airfoil surface are depicted in Figure 6. As shown in Figure 6, the calculated pressure coefficient distributions on both initial and adaptive meshes compare well with the numerical result of Hwang and Yang [34] in which the locally implicit total variation diminishing scheme was used. It is apparent that accurate and high-resolutional result is obtained on the adaptive mesh.

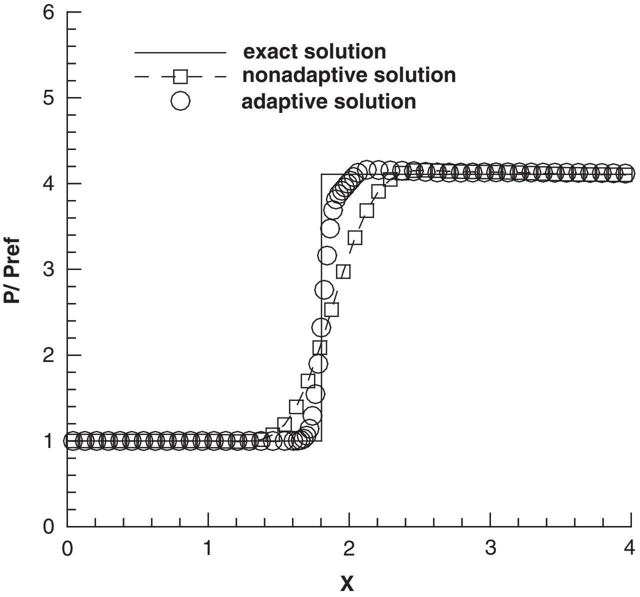

Figure 3. Pressure distributions along the wall for oblique shock reflection at a wall.

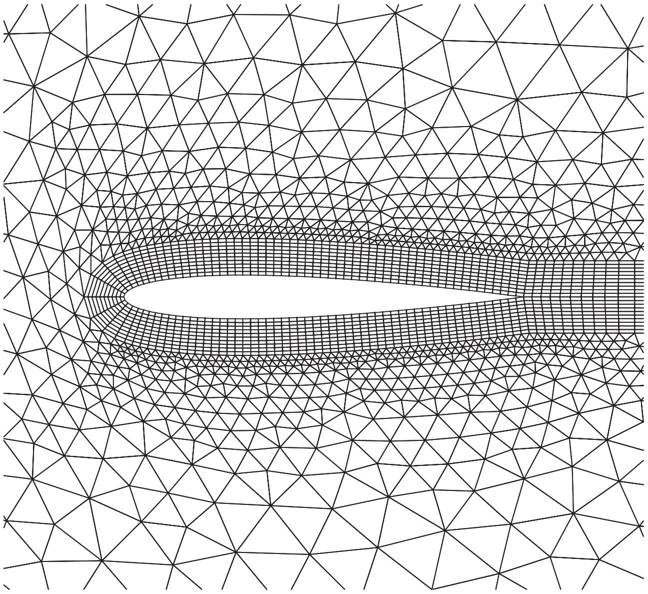

Figure 4. Initial mesh of transonic flow around an NACA 0012 airfoil (4688 cells).

### 5.3. *Transonic flows over vibrating blades with interblade phase angles*

In the present calculations of flows over vibrating blades with interblade phase angles, the inlet Mach number and exit pressure ratio (static exit pressure divided by total pressure) are

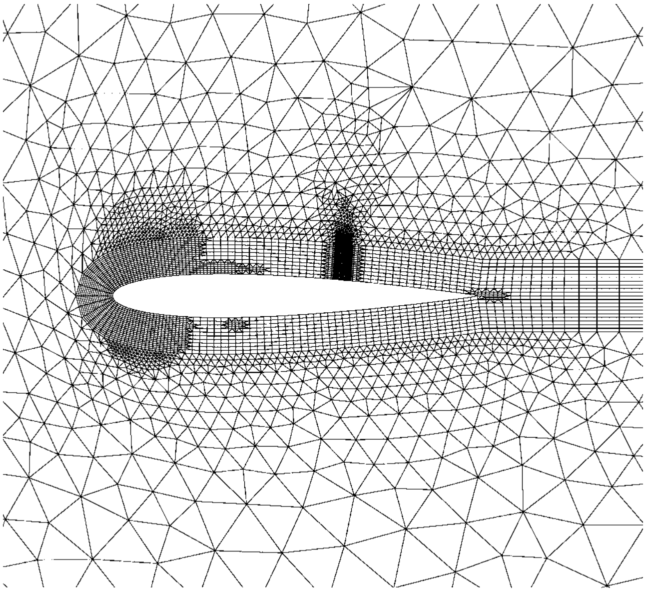

Figure 5. Adaptive mesh of transonic flow around an NACA 0012 airfoil (7150 cells).

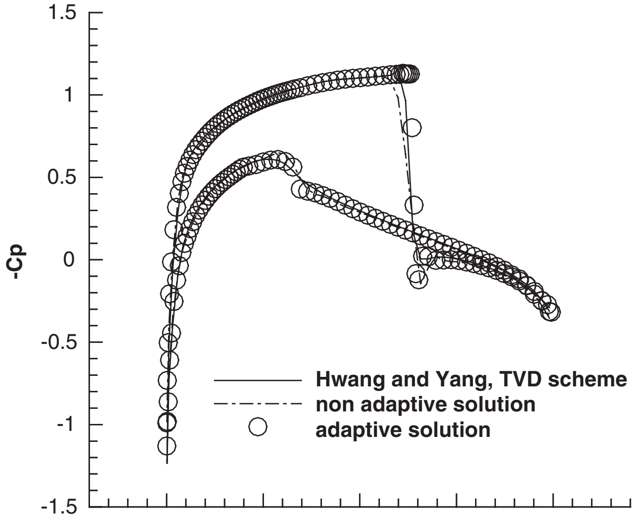

Figure 6. Pressure coefficient distributions for transonic flow around an NACA 0012 airfoil.

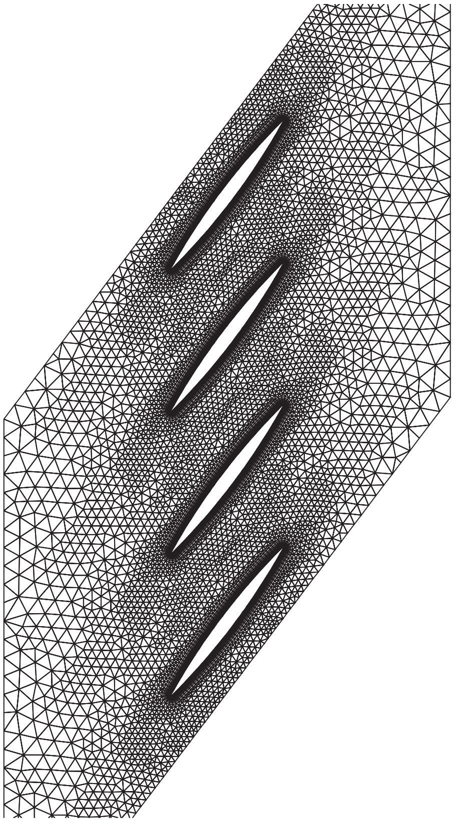

Figure 7. Initial quadrilateral–triangular mesh (13 830 cells) for the transonic flow over vibrating blades.

set to be 0.8 and 0.7322, respectively. The computational domain contains four uncambered biconvex blades, where the values of thickness-to-chord ratio, solidity (chord length divided by blade pitch), and stagger angle are 0.076, 1.3, and 53°, respectively. The motion of these four vibrating blades, which is executing torsional mode oscillations about mid-chord, is governed by the following relation:

$$\alpha = \alpha_0 + \alpha_{\mathrm{I}} \sin(2Mk\tau + m\sigma) \tag{17}$$

where $\alpha$, $\alpha_0$, $\alpha_{\mathrm{I}}$, $M$, $k$, $\tau$ and $\sigma$ represent instantaneous angle of attack, mean flow angle of attack, oscillation amplitude, inlet Mach number, reduced frequency, non-dimensionalized time scale and interblade phase angle, respectively. The blade number $m = 0$, 1, 2 and 3 represent each blade from the lowest to the highest one, respectively. On the initial quadrilateral–triangular mesh (Figure 7), a layer of O-typed quadrilaterals is generated around each blade surface to match the experimental geometry [38], where the leading and trailing edges are rounded with a small radius of curvature (0.33% of chord length). After creating the quadrilaterals, the unstructured triangles are distributed elsewhere according to the mesh generation technique [19]. This quadrilateral–triangular mesh contains 13 830 cells and 9619 nodes, where a layer of O-typed grids with $118 \times 10$ quadrilaterals is generated around each blade.

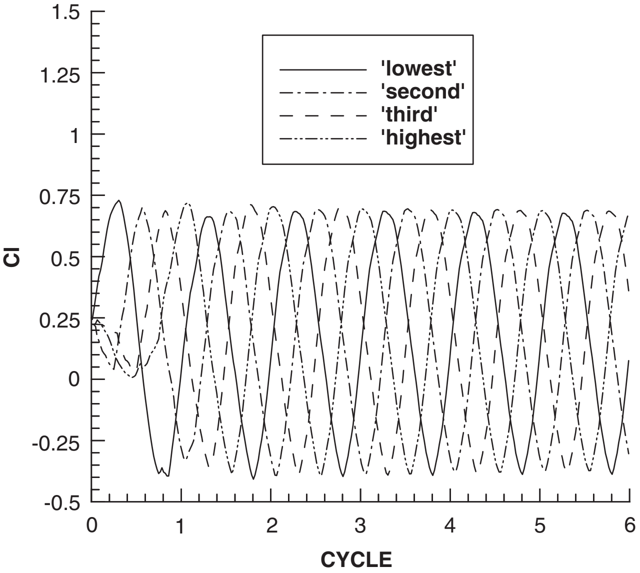

Figure 8. Time history of lift coefficient for the transonic flow over vibrating blades ($M = 0.8$, $\sigma = -90^\circ$, $k = 0.462$, $\alpha_0 = 7^\circ$ and $\alpha_I = 4.8^\circ$).

Considering the first cycle of blade motion for $\sigma$ equal to $-90^\circ$, only the lowest blade ($m = 0$) is set to motion at the beginning, whereas the second ($m = 1$), the third ($m = 2$) and the highest ($m = 3$) blades are set to motion when $2Mk\tau$ reaches $\pi/2$, $\pi$ and $3\pi/2$, respectively. As for $\sigma$ replaced by $90^\circ$, the lowest blade ($m = 0$) is still set to motion at the beginning of the first cycle of motion, whereas the highest ($m = 3$), the third ($m = 2$), and the second ($m = 1$) blades are set to motion when $2Mk\tau$ reaches $\pi/2$, $\pi$ and $3\pi/2$, respectively. Once the blade is set to motion, it will continue its motion until the end of computation. For the transonic flow over vibrating blades with $\sigma$, $k$, $\alpha_0$ and $\alpha_I$ equal to $-90^\circ$, 0.462, $7^\circ$ and $4.8^\circ$, respectively, a constant marching time step of $\Delta\tau = 0.00236$ is chosen. The periodic solution is achieved by processing six cycles of motion, and it takes 3600 time steps to accomplish one cycle of motion. In this computation, $C_1$ and $C_2$ are set to be 0.6 and 1.8, respectively, and adaptation is performed every 30 time steps. From the time history of lift coefficient shown in Figure 8, the periodic characteristic is quickly achieved. The convergence of the present numerical approach on transient, adaptive problems is demonstrated. When one value of $\alpha_I$ ($1.2^\circ$) and two values of $\sigma$ ($-90^\circ$ and $90^\circ$) are chosen, magnitude distributions of the first harmonic dynamic surface pressure difference coefficient $\Delta C_p$ are plotted in Figure 9. To assess the present adaptive solver, the experimental data [38] and related Euler solutions obtained on the non-adaptive quadrilateral–triangular mesh [6] are adopted for comparison. By choosing the experimental data as the reference values, the distributions of magnitude in Figure 9 indicate that the present adaptive solver provides better results than does the related non-adaptive approach, and the present adaptive solutions compare very well with the experimental data. Consequently, the accuracy of the present adaptive approach is confirmed.

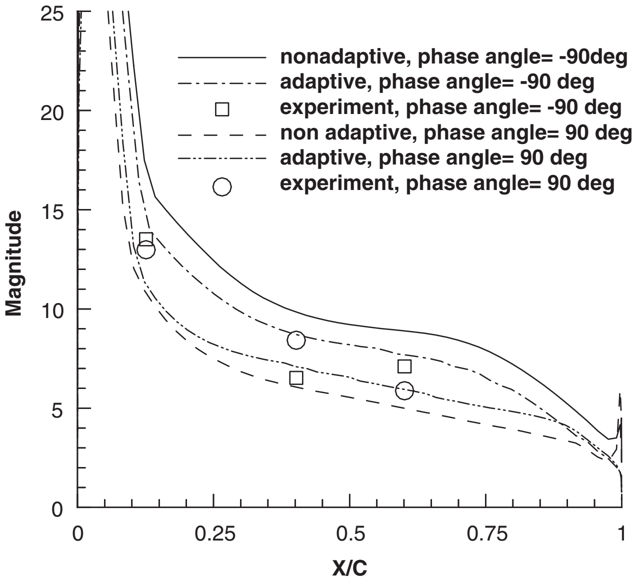

Figure 9. Magnitude distributions of the first harmonic dynamic surface pressure difference coefficient $\Delta C_\mathrm{p}$ for the transonic flow over vibrating blades ($M=0.8$, $k=0.462$, $\alpha_0=7°$ and $\alpha_\mathrm{I}=1.2°$).

As for the case with $\sigma$, $k$, $\alpha_0$ and $\alpha_\mathrm{I}$ equal to 90°, 0.462, 7° and 4.8°, respectively, the instantaneous meshes, pressure contours and vorticity contours during the sixth cycle ($(2MK\tau{-}10\pi)=0$, $\pi/6$, $\pi/3$ and $\pi/2$) are plotted in Figures 10–12. After comparing the instantaneous meshes (Figures 10(a) and 10(d)), pressure contours (Figures 11(a) and 11(d)) and vorticity contours (Figures 12(a) and 12(d)), it is observed that the flow behaviours repeat and proceed one pitch distance in the downward direction for quarter time period. From the results given in Figures 10(a) and 11(a), shocks appear on the front part of upper surface of the second blade, and on the mid-chord of upper surface of the third blade. Meanwhile, two compression waves on the upper leading edge of the lowest blade and on the rear part of the lower surface of the highest blade are observed. Within the passage between the lowest and highest blades, a strong shock is depicted, whose strength is strong enough to choke the flowfield. Considering the vorticity contour shown in Figure 12(a), zones of stronger vorticity gradient shed from the trailing edges of the second and highest blades, whereas zones of minor vorticity gradient shed from the trailing edges of the lowest and third blades. On the upper surfaces of the second and third blades and on the rear part of upper surface of the highest blade, zones of stronger vorticity gradient come into view, whereas zones of minor vorticity gradient on the lower surfaces of the lowest and highest blades are also demonstrated. A vortex located between the downstream of the lowest and second blades, which originally sheds from the trailing edge of the lowest blade, is also observed. Furthermore, there are corresponding zones of strong vorticity gradient, whose locations are the same as those of unsteady shocks in Figure 11(a).

To further investigate the unsteady flowfield during each quarter time period, Figures 10(a)–10(d), 11(a)–11(d) and 12(a)–12(d) are studied. During time evolution, a compression wave

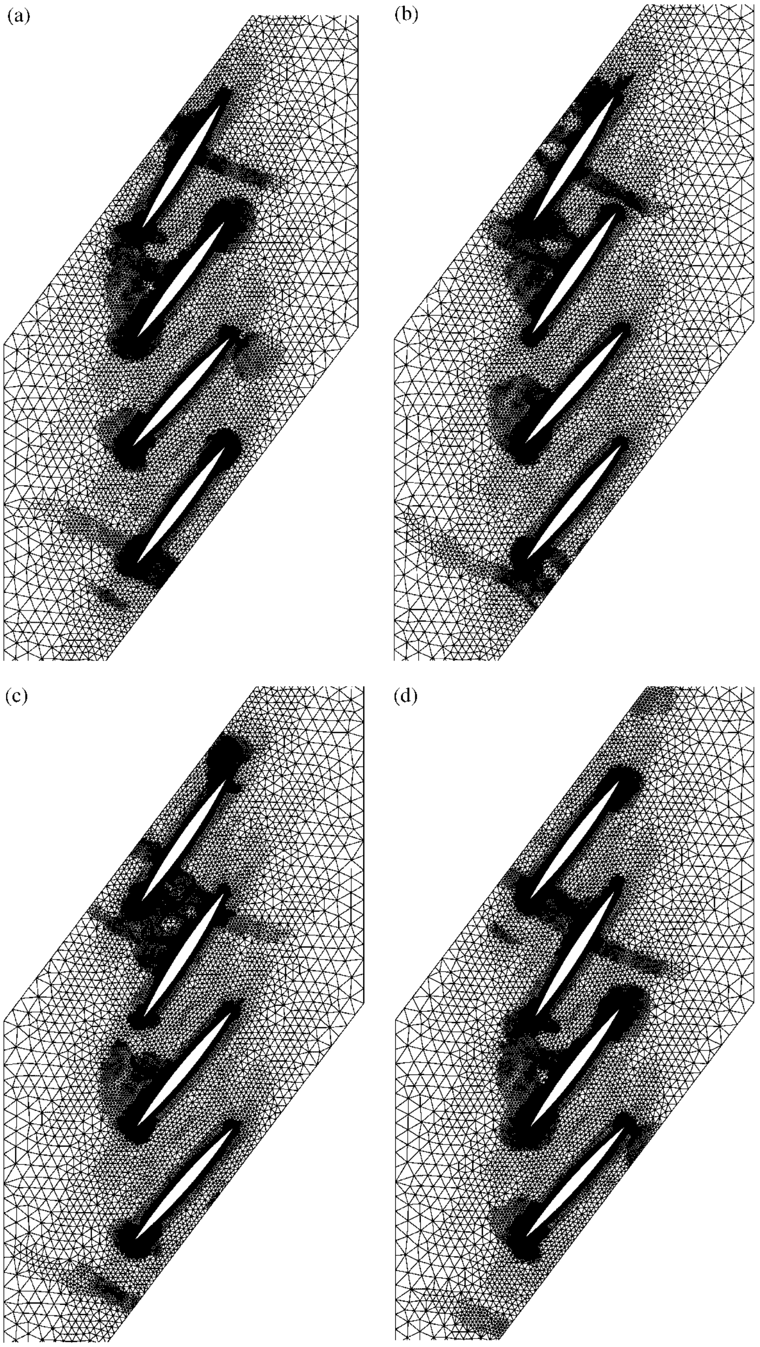

Figure 10. Instantaneous meshes for the transonic flow over vibrating blades ($M = 0.8$, $\sigma = 90^\circ$, $k = 0.462$, $\alpha_0 = 7^\circ$ and $\alpha_I = 4.8^\circ$). ($2MK\tau - 10\pi$) equal to (a) 0, (b) $\pi/6$, (c) $\pi/3$ and (d) $\pi/2$.

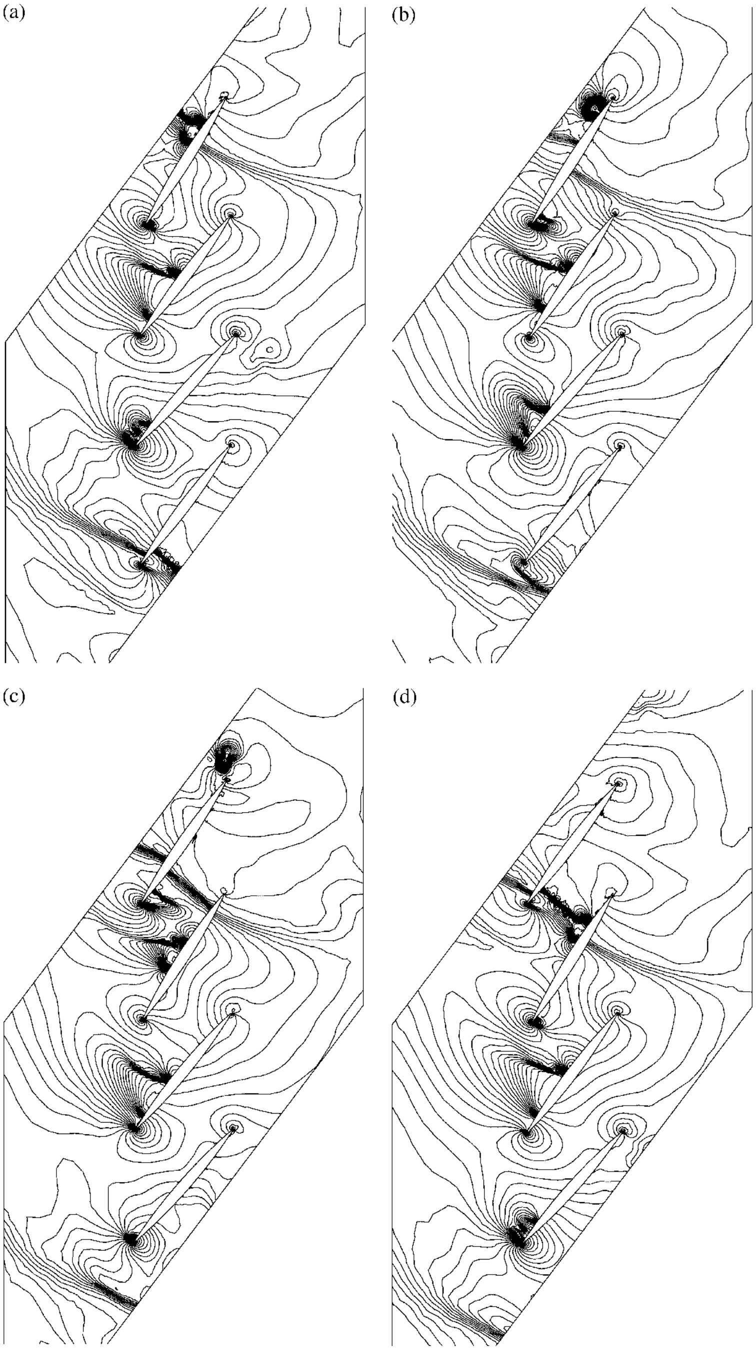

Figure 11. Instantaneous pressure contours for the transonic flow over vibrating blades ($M=0.8$, $\sigma=90°$, $k=0.462$, $\alpha_0=7°$ and $\alpha_{\mathrm{I}}=4.8°$). ($2MK\tau$–$10\pi$) equal to (a) 0, (b) $\pi/6$, (c) $\pi/3$ and (d) $\pi/2$.

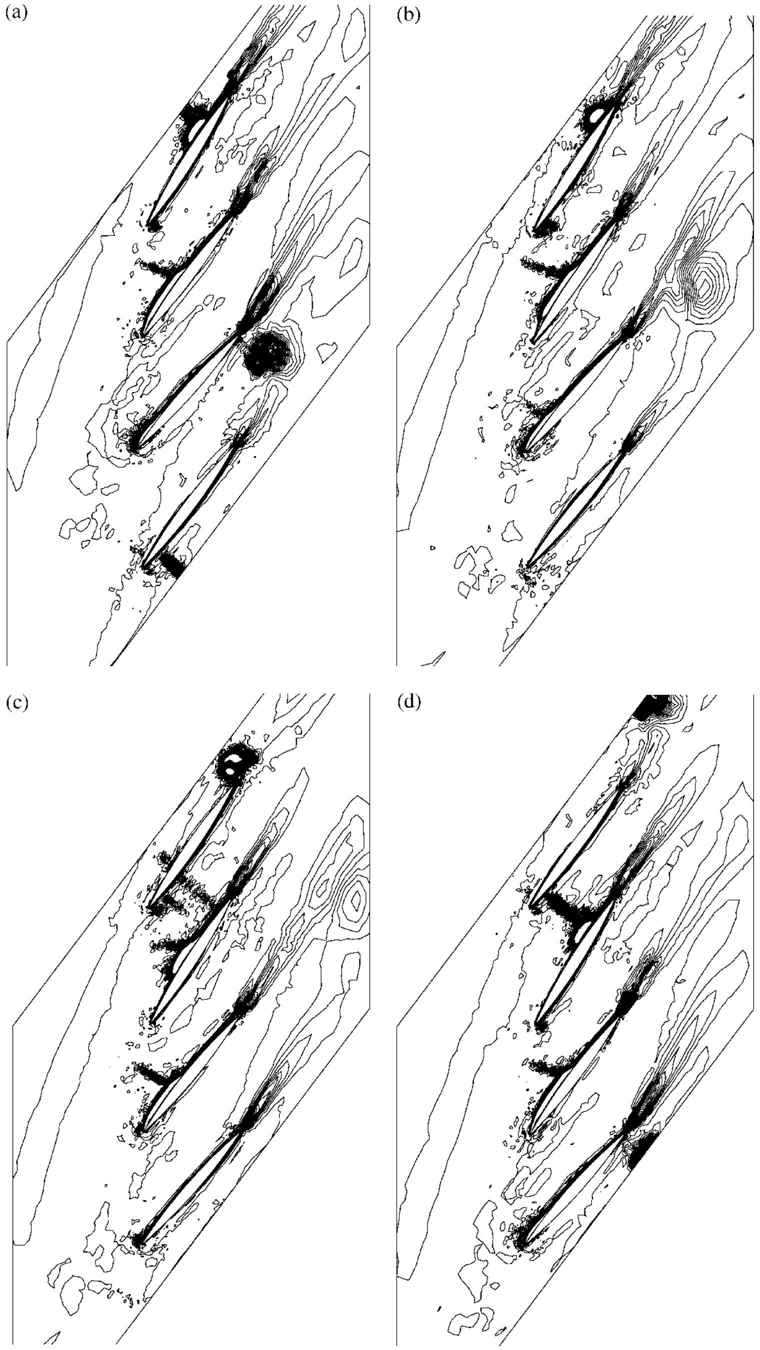

Figure 12. Instantaneous vorticity contours for the transonic flow over vibrating blades ($M = 0.8$, $\sigma = 90°$, $k = 0.462$, $\alpha_0 = 7°$ and $\alpha_I = 4.8°$). ($2MK\tau$–$10\pi$) equal to (a) 0, (b) $\pi/6$, (c) $\pi/3$ and (d) $\pi/2$.

on the upper leading edge of the lowest blade (Figures 10(a) and 11(a)) moves upstream. At the same time, a shock on the front part of lower surface of the lowest blade (Figures 10(a) and 11(a)) moves forward and becomes a strong compression wave. This strong compression wave passes through the leading edge and combines with the upper compression wave (Figures 10(b) and 11(b)). Then this compression wave continues to go upstream (Figures 10(c) and 11(c)) and decreases its strength (Figures 10(d) and 11(d)). A shock on the front part of upper surface of the second blade (Figures 10(a) and 11(a)) moves downstream and becomes stronger (Figures 10(b)–10(d) and 11(b)–11(d)). Meanwhile, a weaker leading edge shock on the lower surface of the highest blade (Figures 10(a) and 11(a)) grows to be stronger and moves downstream (Figures 10(b) and 11(b)). After interaction with the shock standing near the mid-chord of upper surface of the third blade (Figures 10(c) and 11(c)), a stronger shock is formed (Figures 10(d) and 11(d)). At this moment, the flow within the passage between the highest and third blades is choked by this shock.

Comparing Figures 10(a)–10(d) and 12(a)–12(d), a vortex appears between the downstream of the lowest and second blades (Figures 10(a) and 12(a)), and it originally sheds from the trailing edge of the lowest blade. This vortex convects rearward and interacts with the zone of strong vorticity gradient shedding from the trailing edge of the second blade, and eventually goes out of the computational domain (Figures 10(b)–10(d)). Meanwhile, a zone of strong vorticity gradient located on the rear part of upper surface of the highest blade (Figures 10(a) and 12(a)) moves rearward (Figures 10(b) and 12(b)), and it becomes a vortex shedding from the trailing edge of the highest blade (Figures 10(c) and 12(c)). This shedding vortex convects further downstream (Figures 10(d) and 12(d)). The vortex originally shedding from the trailing edge of the highest blade (Figures 10(d) and 12(d)) is the same as that originally shedding from the trailing edge of the lowest blade (Figures 10(a) and 12(a)). Within the passage between the third and highest blades, the unsteady structure of vorticity contours (Figures 12(a)–12(d)) is similar to that of pressure contours (Figures 11(a)–11(d)). During this quarter time period, a zone of high vorticity gradient on the trailing edge of the lowest blade convects and stretches further downstream. From the above discussion and Figure 10, it is obvious that the present adaptive meshes clearly capture the unsteady wave behaviours and vortex-shedding phenomena.

In order to study the effect of the interblade phase angle upon transonic flows over vibrating blades, $\sigma$ is replaced by $-90°$ while $k$, $\alpha_0$ and $\alpha_I$ are set to be 0.462, 7° and 4.8° respectively. The instantaneous meshes, pressure contours and vorticity contours during the sixth cycle ($(2MK\tau - 10\pi) = 0$, $\pi/6$, $\pi/3$ and $\pi/2$) are plotted in Figures 13–15. After comparing the instantaneous meshes (Figures 13(a) and 13(d)), pressure contours (Figures 14(a) and 14(d)) and vorticity contours (Figures 15(a) and 15(d)), it is observed that the flow behaviours repeat and proceed one pitch distance in the upward direction for quarter time period. From the sequence of results given in Figures 13(a)–13(d) and Figures 14(a)–14(d), a shock on the lower surface of the lowest blade (Figures 13(a) and 14(a)) keeps moving close to the leading edge (Figures 13(b) and 14(b)) and eventually passes through the leading edge to form a weak shock on the upper surface of the lowest blade (Figures 13(d) and 14(d)). Initially, there is no shock between the lowest and the second blades in Figures 13(a) and 14(a). A shock on the upper surface of the second blade (Figures 13(a) and 14(a)) moves close to the leading edge, and then goes around the leading edge (Figures 13(b) and 14(b)) to interact with the pressure wave. Eventually, two shocks on the lower surface of the second blade and on the mid-chord of the upper surface of the lowest blade (Figures 13(d) and 14(d))

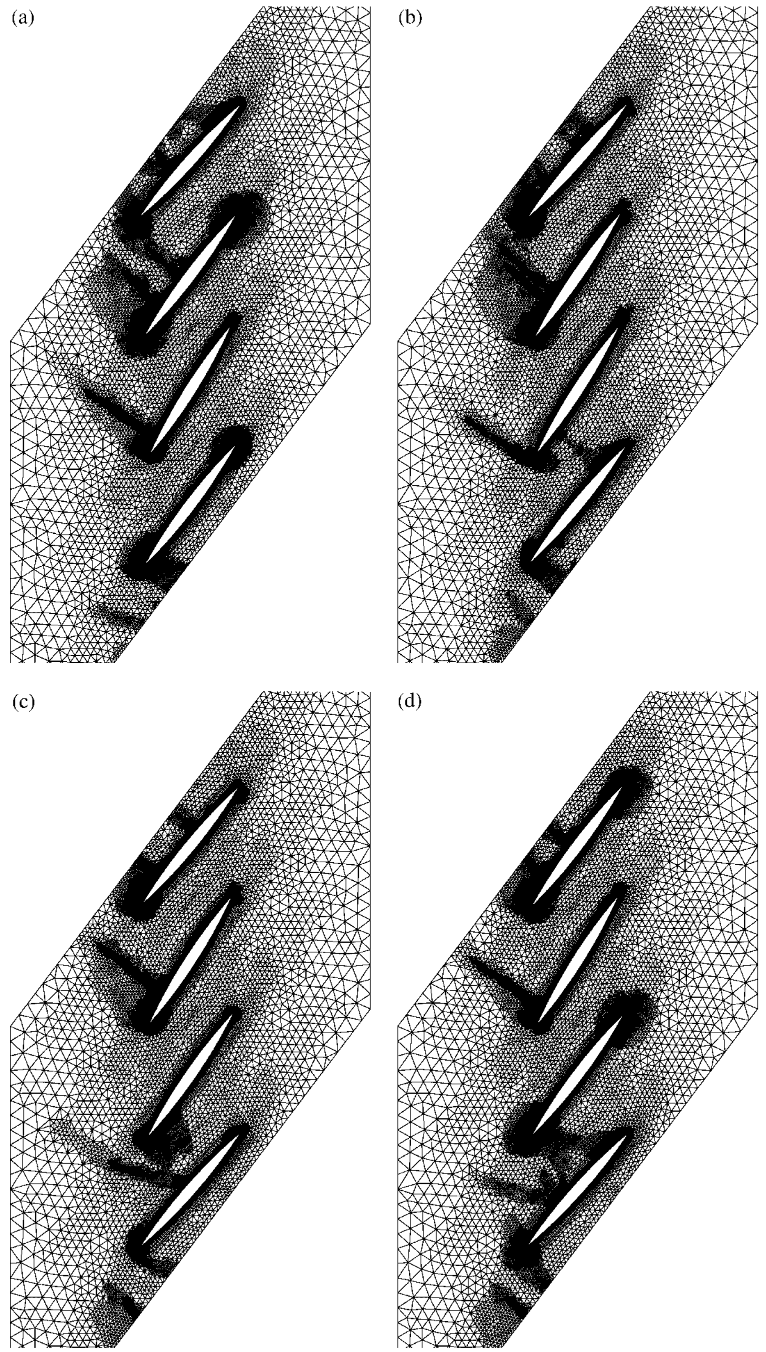

Figure 13. Instantaneous meshes for the transonic flow over vibrating blades ($M = 0.8$, $\sigma = -90^\circ$, $k = 0.462$, $\alpha_0 = 7^\circ$ and $\alpha_I = 4.8^\circ$). ($2MK\tau$–$10\pi$) equal to (a) 0, (b) $\pi/6$, (c) $\pi/3$ and (d) $\pi/2$.

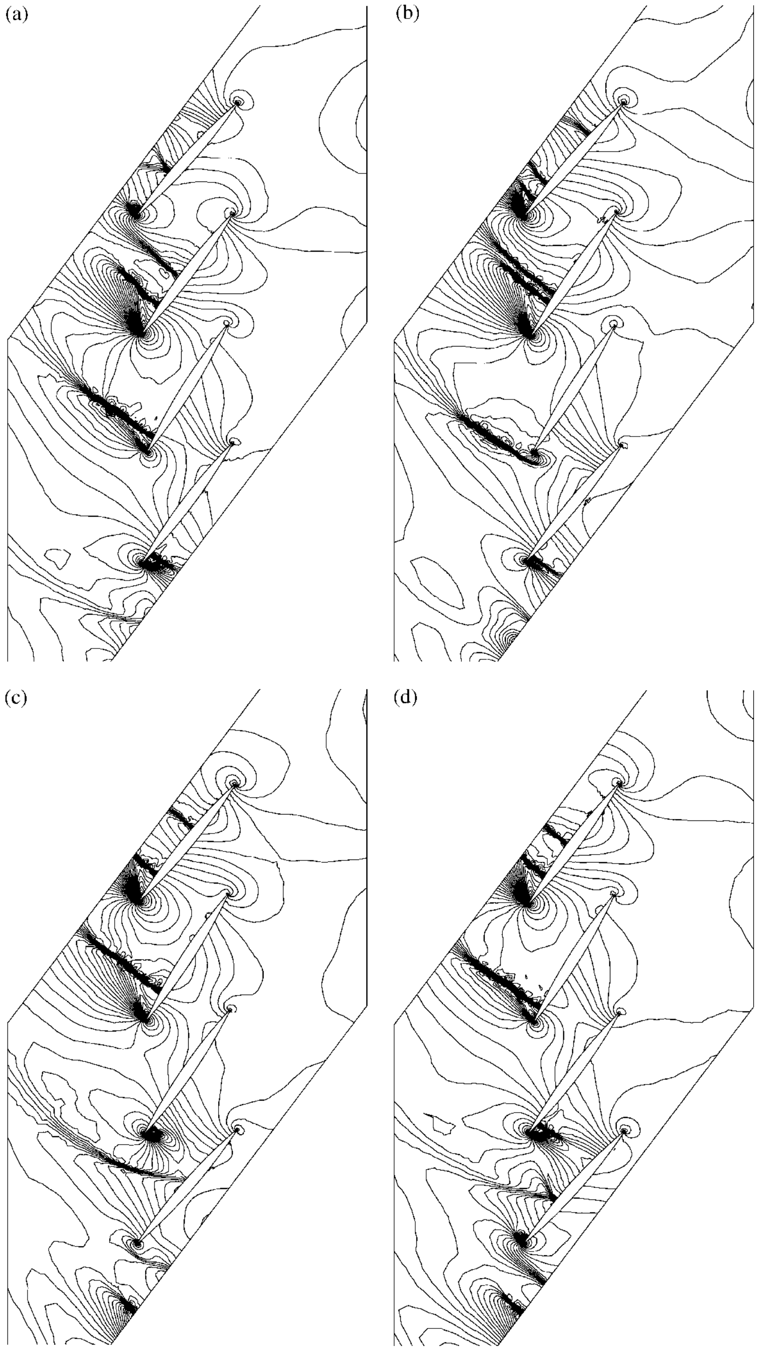

Figure 14. Instantaneous pressure contours for the transonic flow over vibrating blades ($M = 0.8$, $\sigma = -90^\circ$, $k = 0.462$, $\alpha_0 = 7^\circ$ and $\alpha_I = 4.8^\circ$). ($2MK\tau - 10\pi$) equal to (a) 0, (b) $\pi/6$, (c) $\pi/3$ and (d) $\pi/2$.

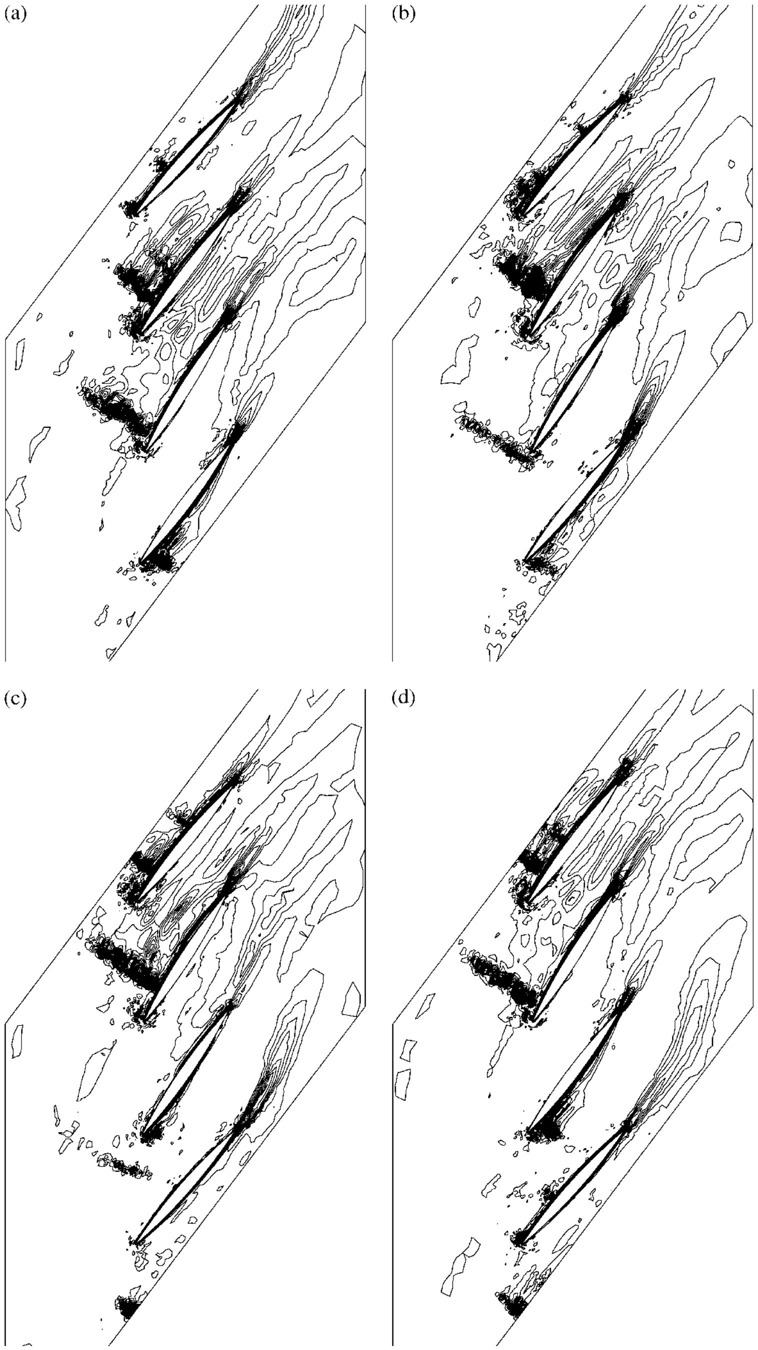

Figure 15. Instantaneous vorticity contours for the transonic flow over vibrating blades ($M = 0.8$, $\sigma = -90°$, $k = 0.462$, $\alpha_0 = 7°$ and $\alpha_I = 4.8°$). ($2MK\tau$–$10\pi$) equal to (a) 0, (b) $\pi/6$, (c) $\pi/3$ and (d) $\pi/2$.

are formed. As shown in Figures 13(a) and 14(a), there are one shock and one compression wave on the upper surface of the third blade. The latter compression wave moves close to the former shock, and eventually combines together to form a stronger shock on the upper surface of the third blade (Figures 13(c) and 14(c)). This stronger shock keeps moving upstream to be close to the leading edge (Figures 13(d) and 14(d)). On the upper surface of the highest blade in Figures 13(a) and 14(a), there exist a weak leading edge shock, a shock on the mid-chord and a rear compression wave. During time evolution, this weak leading edge shock goes downstream (Figure 13(b) and 14(b)) and combines with the mid-chord shock, which is moving upstream. Then a strong shock is formed on the upper surface of the highest blade (Figures 13(d) and 14(d)). Meanwhile, the rear compression wave merges to be stronger (Figures 13(b) and 14(b)), and it keeps moving upstream (Figures 13(d) and 14(d)).

Considering the vorticity contour depicted in Figure 15(a), a zone of vorticity gradient sheds from the trailing edge of each blade. On the upper surfaces of the second, third and highest blades, zones of vorticity gradient come into view. Moreover, zones of vorticity gradient appear on the lower surfaces of the lowest and highest blades. As shown in Figure 15(a), there are corresponding zones of vorticity gradient whose locations are similar to those of unsteady shocks in Figure 14(a).

As far as the sequence of vorticity contours in Figures 15(a)–15(d) is concerned, a zone of vorticity gradient on the lower surface of the lowest blade convects downstream and sheds from the trailing edge. Meanwhile, a zone of vorticity gradient gradually develops on the upper surface of the lowest blade. On the upper surface of the second blade, a zone of vorticity gradient moves rearward and sheds from the trailing edge, whereas a zone of vorticity gradient comes into view on the lower surface of second blade. As shown in Figure 15(a), a strong vorticity gradient standing on the fore portion of upper surface of the second blade moves forward and passes through the leading edge of the second blade (Figure 15(b)). It continues to move forward and decay it is strength (Figures 15(c) and 15(d)). The structure of strong vorticity gradient standing on the fore part of upper surface of the third blade (Figure 15(a)) is similar to that of the corresponding shock and compression wave in Figure 14(a). During time evolution, the migration of strong vorticity gradient (Figures 15(b)–15(d)) looks much like that of the corresponding shock and compression wave (Figures 14(b)–14(d)). On the upper surface of the highest blade, a zone of vorticity gradient becomes stronger (Figures 15(a)–15(d)), whereas a zone of vorticity gradient on the lower surface of the highest blade becomes weaker. The migration of vorticity gradient standing on the front part of upper surface of the highest blade in Figures 15(a)–15(d) is similar to that of the corresponding shock behavior in Figures 14(a)–14(d).

## 6. CONCLUSIONS

The main contribution of this paper is to develop an error indicator and a locally implicit scheme with anisotropic dissipation model on dynamic quadrilateral–triangular mesh. In the Cartesian co-ordinate system, the unsteady Euler equations with moving domain effects are solved to investigate the transonic flows over vibrating blades with interblade phase angles. After performing two flow calculations, which include the oblique shock reflection at a wall and transonic flow around an NACA 0012 airfoil, the accuracy of the locally implicit scheme with anisotropic dissipation model is confirmed. As demonstrated in the instantaneous pressure and vorticity contours, the flow behaviours repeat and proceed one pitch distance in the downward or upward direction for interblade phase angle equal to 90° or −90°, respectively. From the comparison and discussion of instantaneous meshes with pressure and vorticity contours, it is evident that the present adaptive meshes clearly capture the unsteady wave behaviours and vortex-shedding phenomena.

## REFERENCES

1. Usab WJJr, Verdon JM. Advances in the numerical analysis of linearized unsteady cascade flows. *Journal of Turbomachinery* 1991; **113**(4):633–643.
2. Hall KC, William SC. Linearized Euler predictions of unsteady aerodynamic loads in cascades. *AIAA Journal* 1993; **31**(3):540–550.
3. Wolff JM, Fleeter S. Single-passage Euler analysis of oscillating cascade aerodynamics for arbitrary interblade phase. *Journal of Propulsion and Power* 1994; **10**(5):690–697.
4. He L. An Euler solution for unsteady flows around oscillating blades. *Journal of Turbomachinery* 1990; **112**(4):714–722.
5. Huff DL. Numerical analysis of flow through oscillating cascade sections. *Journal of Propulsion and Power* 1992; **8**(4):815–822.
6. Hwang CJ, Yang SY. Inviscid analysis of transonic oscillating cascade flows using a dynamic mesh algorithm. *Journal of Propulsion and Power* 1995; **11**(3):433–440.
7. Gerolymos GA, Vallet I. Validation of three-dimensional Euler methods for vibrating cascade aerodynamics. *Journal of Turbomachinery* 1996; **118**(3):771–782.
8. Ayer TC, Verdon JM. Validation of a nonlinear unsteady aerodynamic simulator for vibrating blade rows. *Journal of Turbomachinery* 1998; **120**(1):112–121.
9. Swafford TW, Loe DH, Huff DL, Huddleston DH, Reddy, TSR. The evolution of NPHASE: Euler/Navier–Stokes computations of unsteady two-dimensional cascade flow fields. *AIAA Paper No*. 94-1834, 1994.
10. He L, Denton JD. Three-dimensional time-marching inviscid and viscous solutions for unsteady flows around vibrating blades. *Journal of Turbomachinery* 1994; **116**(3):469–476.
11. He L. Unsteady flow in oscillating turbine cascade part 2. Computational study. *ASME Paper No*. 96-GT-375, 1996.
12. Abhari RS, Giles M. A Navier–Stokes analysis of airfoils in oscillating transonic cascades for the prediction of aerodynamic damping. *Journal of Turbomachinery* 1997; **119**(1):77–84.
13. Verdon JM. Review of unsteady aerodynamic methods for turbo-machinery aeroelastic and aeroacoustic applications. *AIAA Journal* 1993; **31**(2):235–250.
14. Wolff JM, Fleeter S. Nonlinear separated inviscid-viscous analysis of oscillating cascade aerodynamics using an inverse integral method. *ASME Paper No*. 97-GT-85, 1997.
15. Frey KK, Fleeter S. Oscillating airfoil aerodynamics of a rotating compressor blade row. *Journal of Propulsion and Power* 2001; **17**(2):232–239.
16. Sheng C, Whitfield DL, Anderson WK. Multiblock approach for calculating incompressible fluid flows on unstructured grids. *AIAA Journal* 1999; **37**(2):169–176.
17. Mavriplis DJ. Viscous flow analysis using a parallel unstructured multigrid solver. *AIAA Journal* 2000; **38**(11):1243–1251.
18. Rausch RD, Batina JT, Yang HTY. Spatial adaptation of unstructured meshes for unsteady aerodynamic flow computations. *AIAA Journal* 1992; **30**(5):1243–1251.
19. Hwang CJ, Wu SJ. Global and local remeshing algorithms for compressible flows. *Journal of Computational Physics* 1992; **102**(1):98–113.
20. Webster BE, Shephard MS, Rusak Z, Flaherty JE. Automated adaptive time-discontinuous finite element method for unsteady compressible airfoil aerodynamics. *AIAA Journal* 1994; **32**(4):748–757.
21. Braaten ME, Connell SD. Three-dimensional unstructured adaptive multigrid scheme for the Navier-Stokes equations. *AIAA Journal* 1996; **34**(2):281–290.
22. Delanaye M, Essers JA. Quadratic-reconstruction finite volume scheme for compressible flows on unstructured adaptive grids. *AIAA Journal* 1997; **35**(4):631–639.
23. Parthasarathy V, Kallinderis Y. Adaptive prismatic-tetrahedral grid refinement and redistribution for viscous flows. *AIAA Journal* 1996; **34**(4):707–716.
24. Pirzadeh SZ. A solution-adaptive unstructured grid method by grid subdivision and local remeshing. *AIAA Journal* 2000; **37**(5):818–824.
25. Walsh PC, Zingg DW. Solution adaptation of unstructured grids for two-dimensional aerodynamic computations. *AIAA Journal* 2001; **39**(5):831–837.

26. Mavriplis DJ. Adaptive meshing techniques for viscous flow calculations on mixed element unstructured meshes. *International Journal for Numerical Methods in Fluids* 2000; **34**:93–111.
27. Yang SY. Adaptive analysis of the inviscid supersonic flow over a backward-facing step. *Journal of Propulsion and Power* 2001; **17**(4):938–940.
28. Jameson A, Schmidt W, Turkel E. Numerical solutions of the Euler equations by finite volume methods using Runge–Kutta time-stepping schemes. *AIAA Paper No*. 81-1259, 1981.
29. Mavriplis DJ. Accurate multigrid solution of the Euler equations on unstructured and adaptive meshes. *AIAA Journal* 1990; **28**(2):213–221.
30. Hwang CJ, Liu JL. Inviscid and viscous solutions for airfoil/cascade flows using a locally implicit algorithm on adaptive meshes. *Journal of Turbomachinery* 1991; **113**(4):553–560.
31. Reddy KC, Jacock JL. A locally implicit scheme for the Euler equations. *AIAA Paper No*. 87-1144, 1987.
32. Nayani SN. A locally implicit scheme for Navier–Stokes equations. *Ph.D. Thesis*, The University of Tennessee, Knoxville, Tennessee, 1988.
33. Hwang CJ, Fang JM. Solution-adaptive approach for unsteady flow calculations on quadrilateral-triangular meshes. *AIAA Journal* 1996; **34**(4):851–853.
34. Hwang CJ, Yang SY. Locally implicit total variation diminishing schemes on mixed quadrilateral-triangular meshes. *AIAA Journal* 1993; **31**(11):2008–2015.
35. Giles MB. Nonreflecting boundary conditions for Euler equation calculations. *AIAA Journal* 1990; **28**(12): 2050–2058.
36. Thomas PD, Lombard CK. Geometric conservation law and its application to flow computations on moving grids. *AIAA Journal* 1979; **17**(10):1030–1037.
37. Marcel V. Analysis of finite-difference and finite-volume formulations of conservation laws. *Journal of Computational Physics* 1989; **81**(1):1–52.
38. Buffum DH, Fleeter S. The aerodynamics of an oscillating cascade in a compressible flowfield. *Journal of Turbomachinery* 1990; **112**(4):759–767.